Solar Cell Photo-Luminescence Modulation for Optical Frequency Identification (OFID) Devices

Walter Daniel Leon-Salas, Member, IEEE, and Xiaozhe Fan

(Invited Paper)

Abstract—This paper presents a wireless optical communication scheme that uses solar cells to transmit information. Transmission of information with a solar cell is possible by exploiting the fact that high-efficiency solar cells are also good at emitting light. These emissions, called luminescent emissions, are a function of the voltage across the cell. Here, we take advantage of this fact to modulate the luminescent emissions of a GaAs solar cell to transmit information. We call devices that use this type of communication Optical Frequency Identification (OFID) devices. A circuit model of a solar cell that includes luminescent emissions is presented along with a circuit that modulates the photo-luminescent radiation emitted by a solar cell while harvesting energy from it. An analysis of this circuit is presented and employed to suggest different modulation strategies. A prototype of the modulator was built and tested. Test results show good agreement with the circuit analysis. It is also shown how the proposed circuit can be used to implement Pulse Amplitude Modulation and On-Off Keying (OOK) modulation. Experimental results show that the proposed communication system achieves a bit error rate of 1.6×10^{-3} at a rate of 10 kbps and at a distance of 50 cm.

Index Terms—luminescence, solar cells, energy harvesting, optical communications.

I. INTRODUCTION

This work presents a communication scheme that uses luminescent emissions of high-efficiency solar cells to transmit information wirelessly. This scheme takes advantage of the fact that, in order to achieve high efficiency, solar cells must also be good emitters of light [1]. GaAs solar cells, for instance, have strong luminescent emissions in the near infrared portion of the electro-magnetic spectrum [2]. Moreover, the intensity of the luminescent emissions from a solar cell is a function of the cell's voltage [3,4]. Hence, luminescent emissions can be modulated to convey information by appropriately varying the solar cell's voltage. These modulated emissions can be detected and decoded by a receiver, or reader, equipped with a photo-detector and the corresponding amplification and decoding circuits.

Solar cells can also receive information encoded optically, by virtue of their photo-transduction property, and convert radiant (light) energy into electrical energy (energy harvesting), which is the intended function of a solar cell. Devices employing this approach can be fully passive, being powered only by their solar cells, yet able to transmit and receive information wirelessly. In this regard, the envisioned devices are analogous to Radio Frequency Identification (RFID) devices.

W. D. Leon-Salas, X. Fan and Y. Wang are with the School of Engineering Technology, Purdue University, West Lafayette, IN, 47907 USA e-mail: wleonsal@purdue.edu.

RFID devices can be fully passive, being energized only by the electro-magnetic field generated by a nearby reader, and are still able to transmit and receive information wirelessly. Due to this analogy with RFID, we call devices based on the proposed communication scheme, Optical Frequency Identification (OFID) devices. As with RFID, OFID devices are not just limited to the transmission of fixed identification codes but can also be employed in sensing and monitoring applications [5.6].

The concept of using solar cells for energy harvesting and for receiving information encoded optically has been explored before using organic [7] and inorganic solar cells [8,9]. In this work, however, solar cells are also employed for the transmission of information. Hence, a device based on the proposed scheme can re-use its on-board solar cell for three purposes, namely, data reception, data transmission and energy harvesting, resulting in overall cost and size savings.

OFID devices can be employed in Internet-of-Things (IoT) applications that require seamless integration of sensors and electronic devices with everyday objects. To be truly seamless, these devices must be able to communicate wirelessly to ease their integration with objects. Moreover, they should be able to harvest ambient energy to avoid frequent recharging or periodic battery replacements. Given that radiant energy is the most abundant and available source of energy, with power densities ranging from 100 mW/cm² for outdoor scenarios and 0.1 mW/cm² for well-lit indoor spaces [10], OFID devices can provide suitable solutions to many IoT applications.

Radio-based communication has been the dominant technology for establishing wireless connectivity in IoT applications. Most existing solutions rely on unlicensed radio bands for ease of deployment and adoption [11,12]. However, these bands are expected to become increasingly crowded as more IoT devices are deployed resulting in higher interference levels and slower throughputs. In this regard, OFID devices are appealing since they can access an unlicensed and mostly unused part of the electro-magnetic spectrum.

The OFID concept was briefly introduced in our previous work [13]. Here, this concept is developed further by presenting a model for luminescent emissions from a solar cell and an electronic circuit suitable for both the modulation of photoluminescent (PL) emissions and energy harvesting with a GaAs solar cell. The rest of this paper is organized as follows: Section II provides a model for the luminescence emissions in solar cells, Section III describes in more detail the OFID concept and lists potential applications. Section IV presents the design and analysis of a PL modulation circuit while section V presents results from a hardware implementation. Section

VI concludes the paper.

II. LUMINESCENCE IN SOLAR CELLS

Luminescence is the emission of light from certain materials, such as semiconductors, under external excitation, and which is not caused by an increase in temperature. PL occurs when the external excitation is provided by light, whereas electro-luminescence (EL) occurs when the external excitation is provided by injected electrical charges. In semiconductors, where there is a conduction band and a valence band separated by an energy band gap, luminescence occurs when electrons from the conduction band transition to the valence band emitting a photon of energy equal to the electron's excess energy.

The PL process is depicted in Fig. 1 for a semiconductor with band gap energy E_g . The energy of an absorbed photon excites an electron from the valence band to the conduction band. When an electron falls back to the valence band, a photon with energy E_g is emitted.

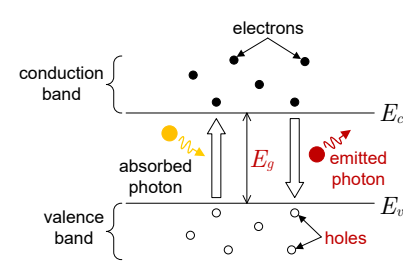


Fig. 1. Photo-luminescence phenomenon in a semiconductor. Absorbed photons create electron-hole pairs. When one of these electrons and holes recombine, a photon with energy E_g is emitted.

Considering that the energy of a photon can be quantified by $E^e_{ph} = hc/\lambda_e$, where h is Planck's constant, c is the speed of light and λ_e is the wavelength, equating E^e_{ph} to E_g allows us to calculate the wavelength of the emitted photons. GaAs has a band gap energy of 1.4 eV resulting in an emitted wavelength of 886.3 nm.

Here we extend the equivalent circuit of a solar cell, as shown in Fig. 2, to include the emitted luminescent radiation. In the figure, Φ_{in} denotes the incident radiant flux, while Φ_{lum} denotes the emitted luminescent radiant flux (with radiant flux measured in Watts). In this equivalent circuit, the diode modeling the "knee" in the current-vs-voltage (IV) curve of a solar cell has been replaced by a light-emitting diode (LED) emitting Φ_{lum} . R_{sh} is the shunt resistance, C_j is the junction capacitance and R_{sr} is the series resistance of the solar cell.

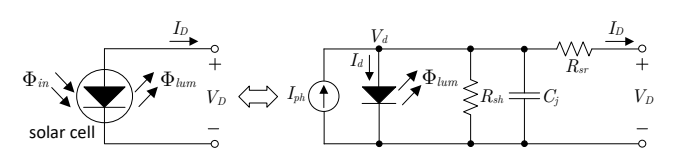


Fig. 2. Single-diode equivalent circuit of a solar cell including emitted luminescent radiation Φ_{lum} .

In the equivalent circuit, I_{ph} is the photo-generated current of the solar cell. For monochromatic light, the value of I_{ph} is given by:

$$I_{ph} = q(1 - R) \ QE(\lambda_i) \ \underbrace{\left(\frac{\Phi_{in}}{E_{ph}^i}\right)}_{\phi_{in}} \tag{1}$$

where, q is the electron's charge, R is the fraction of the photogenerated electrons that recombine inside the solar cell and do not contribute to the current, $QE(\lambda_i)$ is the quantum efficiency at the wavelength of the incident light λ_i , $E^i_{ph} = hc/\lambda_i$ is the energy of an incident photon and ϕ_{in} is the incident photon flux. The current through the LED, I_d , is related to the implied voltage, V_d , by the diode equation:

$$I_d = I_s \left(e^{V_d/nV_T} - 1 \right) \tag{2}$$

where, n is the ideality factor of the diode, V_T is the thermal voltage and I_s is the reverse saturation current.

The luminescent radiant flux emitted by the solar cell has two components. The first component is due to the photogenerated electrons that recombine radiatively and the second component is due to the current I_d that flows through the solar cell:

$$\Phi_{lum} = \underbrace{\eta \ \kappa \ R \ QE(\lambda_i) \ \Phi_{in}}_{\text{first component}} + \underbrace{\eta \ \kappa \ R \ E_{ph}^e \left(\frac{I_d}{q}\right)}_{\text{second component}}$$
(3)

where, η is the fraction of photons generated inside the solar cell that escape the solar cell, i.e. do not get internally reflected or re-absorbed and κ is the fraction of the recombined electrons that recombine radiatively, i.e. generate a photon upon recombination. In the dark, $\Phi_{in}=0$ and the emitted luminescent radiant flux is only due to I_d , that is, due to charges injected into the solar cell (EL).

For most solar cells, $R_{sr} \sim 0$ and $V_d \approx V_D$. Combining (2) and (3) and assuming $V_d \approx V_D$ yields:

$$\Phi_{lum} = \eta \kappa R \left(QE(\lambda_i) \Phi_{in} - \frac{E_{ph}^e I_s}{q} + \frac{E_{ph}^e I_s e^{V_D/nV_T}}{q} \right)$$
(4)

Equation (4) shows an exponential relationship between Φ_{lum} and the external voltage V_D . This relationship is exploited in the OFID concept to modulate the luminescent emissions of a solar cell to convey information.

Of particular interest is the luminescent radiant flux at short circuit (SC), Φ^{sc}_{lum} , open circuit (OC) Φ^{oc}_{lum} and at the maximum power point (MPP) Φ^{mpp}_{lum} . From (3) we obtain:

esolar cell.
$$\Phi_{lum}^{sc} = \eta \kappa R \left(QE \cdot \Phi_{in} \right)$$

$$(5)$$

$$\downarrow I_{B_{sr}} + \Phi_{lum}^{oc} = \eta \kappa R \left(QE \cdot \Phi_{in} - \frac{E_{ph}^{e}I_{s}}{q} + \frac{E_{ph}^{e}I_{s}e^{V_{oc}/nV_{T}}}{q} \right)$$

$$\downarrow C_{j} \quad V_{D} \quad \Phi_{lum}^{mpp} = \eta \kappa R \left(QE \cdot \Phi_{in} - \frac{E_{ph}^{e}I_{s}}{q} + \frac{E_{ph}^{e}I_{s}e^{V_{mpp}/nV_{T}}}{q} \right)$$

where, V_{oc} is the solar cell's open circuit voltage and V_{mpp} is the cell's voltage at the MPP. Considering a large R_{sh} , the

following explicit solutions for V_{oc} and V_{mpp} can be obtained [14]:

$$V_{oc} = nV_T \log \left(\frac{I_{ph} + I_s}{I_s} \right)$$

$$V_{mpp} = nV_T \cdot W \left(\frac{I_{ph} + I_s}{I_s} \cdot e \right) - nV_T$$
(6)

where, $W(\cdot)$ is the Lambert-W function [15].

Fig. 3 shows graphically the relationship between Φ_{lum} and V_D described by (4) for $\eta=0.4$, $\kappa=0.8$, R=0.1, QE=0.8, $I_s=3.506\times 10^{-17}$ A and $\Phi_{in}=1.5$ mW. Marked with circles on the figure are the values of Φ_{lum} for SC, MPP and OC as given by equations (6) and (7).

For $V_D > V_{oc}$, the net current flow is into the solar cell. Hence, for this case, the excitation that stimulates luminescence includes injected charges. In this scenario the solar cell consumes energy instead of generating energy. However, high levels of luminescent radiant flux can be achieved for $V_D > V_{oc}$. The region $V_D < V_{oc}$ corresponds to PL. In this region, the luminescent radiant flux Φ_{lum} can be modulated using different strategies. For instance, the cell can be switched between OC and MPP or OC and SC for On-Off Keying (OOK) modulation. Notice that at the MPP the solar cell harvests the maximum amount of energy. Hence, a modulation scheme that includes the MPP might be preferable in terms of energy harvesting. Pulse Amplitude Modulation (PAM) of the PL radiant flux is also possible by operating the solar cell in the region between OC and MPP or between OC and SC.

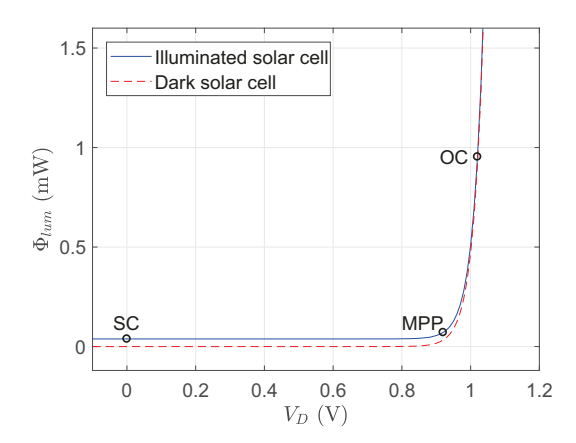


Fig. 3. Luminescent radiant flux emitted by a solar cell, Φ_{lum} , as a function of the voltage across the solar cell V_D as modeled by (4) for the case of an illuminated solar cell and a dark solar cell. The points SC, MPP and OC denote short-circuit, maximum power point and open-circuit conditions, respectively.

The exponential relationship between Φ_{lum} and V_D was verified experimentally using the setup shown in Fig. 4. In this setup, a GaAs solar cell from Alta Devices [16] was placed at a distance of 6.5 cm in front of a red (623 nm) LED flashlight with emitted irradiance of 23.98 mW/cm². An optical power sensor (Thorlabs S120C), with an 850 nm long-pass optical filter in front of it, was placed at the same distance from the solar cell and recorded the radiant flux emitted by the solar cell. This experimental setup was isolated from ambient light to avoid unintended excitations.

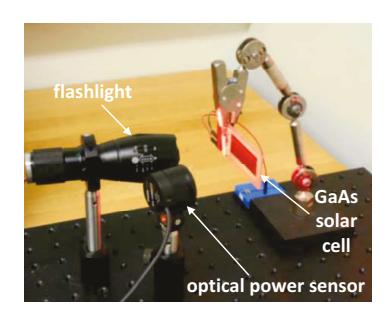


Fig. 4. Experimental setup used to measure the optical power of the luminescent radiation emitted by a GaAs solar cell at a certain distance. A red LED flashlight was employed to illuminate the solar cell.

Fig. 5 shows the measured optical power for an illuminated GaAs solar cell (flashlight on) and for a dark solar cell (flashlight off). The exponential relationship between Φ_{lum} and V_D given in (4) can be observed.

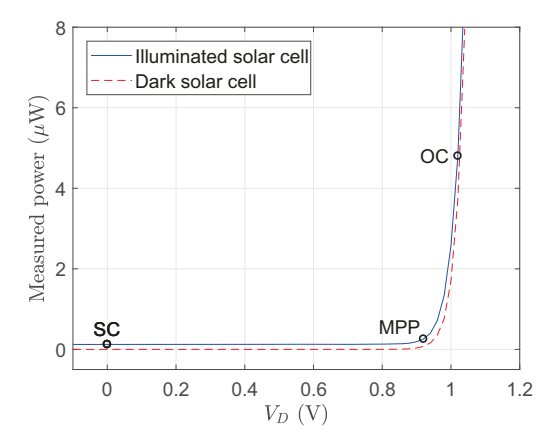


Fig. 5. Measured optical power of the luminescent radiant flux emitted by a GaAs solar cell when illuminated by a red flashlight and in the dark as the voltage across the solar cell V_D is varied.

A visual confirmation of PL and EL emissions was obtained using a night-vision camera sensitive to infrared light. The images captured by the camera are shown in Fig. 6. Fig. 6 (a) shows the solar cell illuminated by the flashlight and with an open circuit between the solar cell terminals (OC PL). Fig. 6 (b) shows the solar cell illuminated by the flashlight while the cell is biased at the MPP (MPP PL). Fig. 6 (c) shows the solar cell illuminated by the flashlight with a short circuit between the cell's terminals (SC PL). Fig. 6 (d) shows the solar cell with the flashlight off while an external voltage of 1.0 V is applied to the cell (EL). From these photos, a significant difference between the luminescent radiation emitted by the solar cell at OC and at MPP or SC can be observed. This observation qualitatively confirms the model and measurements presented above. A strong EL emission can also be observed suggesting that even in complete dark environment, the solar cell can still be employed to transmit information.

III. SYSTEM OVERVIEW

An OFID communication system is conceptually shown in Fig. 7. Communication is between an OFID device and a

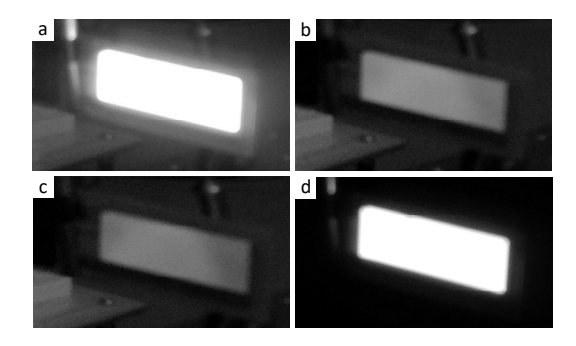


Fig. 6. Images of a GaAs solar cell captured using a night-vision camera for the following conditions: a) flashlight on and open circuit (OC PL); b) flashlight on and cell biased at the MPP (MPP PL); c) flashlight on and short circuit (SC PL) and d) flashlight off and 1.0 V applied to the solar cell terminals (EL).

reader. The figure shows an active reader, that is, a reader that illuminates the solar cell in the OFID device. The light generated by the reader carries radiant energy from the reader to the OFID device to energize and activate the device. To transmit data to the device, the reader modulates the power of the generated light. The reader is also equipped with a photodetector, an amplifier, focusing optics and an optical filter to detect the luminescent radiation emitted by the solar cell.

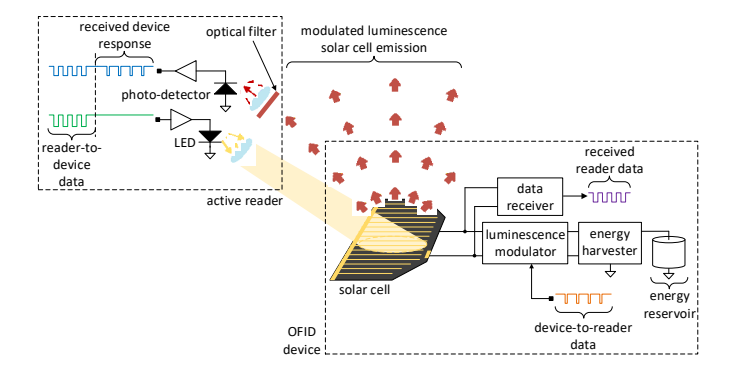


Fig. 7. Conceptual diagram of an OFID communication system consisting of an active reader and an OFID device. The active reader illuminates the solar cell to transmit both energy and data to the device. The OFID device modulates the luminescent emissions of its solar cell to transmit data back to the reader.

The main components of an OFID device are: 1) a data receiver whose function is to demodulate variations in optical power to recover data sent by the reader; 2) a luminescence modulator which modulates the luminescent emissions (PL or EL) of a solar cell to transmit data back to the reader and 3) an energy harvester circuit whose function is to draw out energy from the solar cell to either power up the OFID device directly or to charge an energy reservoir. The energy harvester may also boost and stabilize the output voltage of the cell in order to provide a supply voltage suitable to power the electronic circuits in the OFID device. The energy reservoir, which can be a battery or a super-capacitor, is optional and would be necessary if the OFID device is expected to work when an active reader is not present or there is none or insufficient ambient light to power the device up. Depending on the target

application, an OFID device may be outfitted with a sensor interface, a processor, a timer or a serial communications port.

Another possible configuration of an OFID communication system is depicted in Fig. 8. In this configuration a passive reader is employed. A passive reader does not actively illuminate the solar cell of the OFID device, but instead relies on ambient light to stimulate PL emissions from the solar cell or to charge its energy reservoir. This configuration has the advantage of simplifying the reader complexity, which only needs to be equipped with a photo-detector and the corresponding optics.

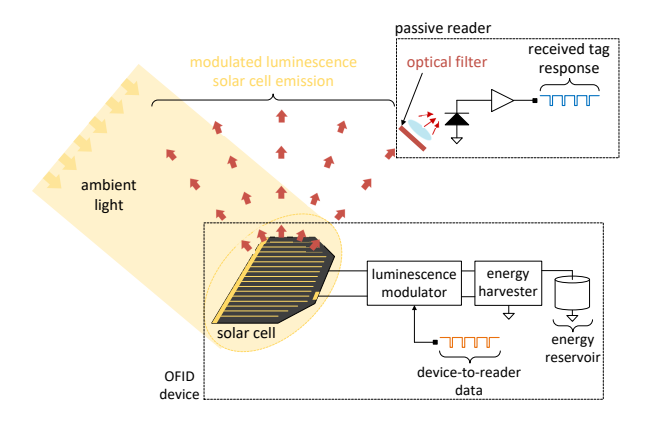


Fig. 8. OFID communication system with passive reader. A passive reader takes advantage of ambient light to generate a PL response. Alternatively, ambient light can be used to charge an energy reservoir. Charges stored in the energy reservoir can be used to stimulate EL emissions by forward biasing the solar cell.

This configuration may be particularly suitable for outdoor settings with direct solar radiation. A drawback of this configuration is that the reader is not able to transmit data to OFID devices. Hence, a passive reader cannot interrogate OFID devices or synchronize their transmissions. In these cases, the devices may initiate a transmission based on events, such as a sensor input crossing a threshold or the expiration of a timer. In dark or not well-lit environments, an OFID device can still transmit information to a passive reader by stimulating EL emissions from its solar cell.

Comparison with RFID

OFID devices are analogous to *passive* RFID devices in that both can be fully passive and get energized by the radiation emitted by a reader. In both cases, the reader modulates its emitted radiation to transmit data to the devices. However, using light instead of radio waves provides unique opportunities to OFID devices.

For instance, OFID devices can harvest energy from ambient light which is a prevalent source of energy in many environments. Hence, unlike RFID, OFID devices can function even if they are not in close proximity to a reader, as long as they are in an environment with sufficient ambient light. Another advantage of OFID is that, light can be collimated in narrow beams using lenses and mirrors. As a result an OFID reader can have very large antenna gains since it can concentrate most of its emitted energy in one direction. To get similar gains for

1 GHz radio signals, for instance, would require an antenna 100 meters long [17].

Imaging receivers or cameras can be used to receive transmissions from multiple OFID devices simplifying the need for collision avoidance mechanisms and dramatically reducing background and mutual optical interference. A high-speed video camera would allow communication at few hundred or thousands of bits per second, which would be acceptable for many identification and sensing applications. Moreover, a camera can pinpoint the exact locations of the OFID devices within its field of view, something that is more challenging to accomplish with radio signals. OFID devices can be placed on or near metallic surfaces without affecting their performance. RFID tags require special mounts to avoid detuning when mounted on metallic surfaces [18] increasing their cost and size. OFID devices can still work inside transparent liquids or underwater. Low-frequency RFID devices can still work underwater but their read range is greatly diminished especially in seawater [19].

OFID devices operating outdoors can use readily-available solar radiation to power themselves up and stimulate PL emissions from their solar cells and modulate them with information. Since light does not generate electromagnetic interference, OFID devices can be used in places, such as hospitals, airplanes and some industrial settings, where electromagnetic interference is of concern.

Like other optical communication systems, an OFID system requires line of sight between the reader and an OFID device for optimal performance. However, non-line-of-sight optical communications are still possible for short ranges using reflected or diffuse light [20].

At present, system-level costs of OFID are higher than RFID. The current cost of a high-efficiency GaAs solar cell with an area of 5 cm × 1.7 cm is around \$20. This cost is much higher than RFID antennas, which can be fabricated for few cents using printing techniques [21,22]. The electronic circuits of an OFID device can be integrated in a single microchip, which is expected to cost as much as an RFID transponder microchip when mass produced. Depending on the application, smaller solar cells could be used to reduce costs. It is expected that the cost of GaAs solar cell will decrease if GaAs cells become more popular or find niche applications such as OFID communications. Costs can also be reduced if OFID devices are reused and not discarded after a single use. The solar cells can be recycled for new devices or other purposes.

At the reader side, high-power LEDs or laser diodes, coupled to low-cost non-imaging optics for beam focusing, can be used as light sources for an *active* OFID reader. On the other hand, the cost of an RFID reader antenna varies depending on its power rating, frequency of operation and reading range and can, in some cases, be more expensive than a high-power LED or a laser diode. The cost of an LED or laser diode driver can be assumed to be similar to that of an RF amplifier. Thus, we expect the cost of an active OFID reader to be comparable to that of an RFID reader and the cost of a passive OFID reader to be lower than that of an RFID reader.

Possible Applications

Fig. 9 shows some potential applications of an OFID communication system. OFID devices can be employed for environmental monitoring (Fig. 9 (a)) if they are equipped with sensors to monitor environmental variables such as water or air contaminants. In this application, solar energy can be used for both powering the sensor and for stimulating PL radiation from the solar cells. An unmanned air vehicle equipped with a passive imaging receiver (high-speed infrared camera) can detect the modulated PL emissions of the solar cells. A camera will be able to receive and spatially separate several transmissions simultaneously. Furthermore, the camera will be able to locate the position of the sensors and determine their location relative to the surroundings.

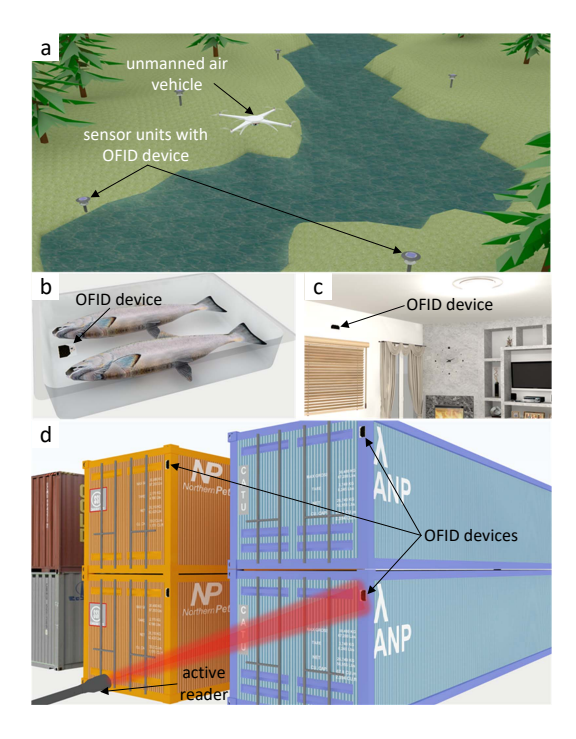


Fig. 9. Possible applications of OFID devices: a) environmental monitoring; b) identification and monitoring of perishable goods; c) smart home monitoring; d) long-range identification of metallic shipping containers.

Another possible application of the OFID devices is tracking and monitoring of perishable goods, such as food or vaccines, throughout the supply chain (Fig. 9 (b)). As a package moves through the supply chain, its presence at different points in the supply chain can be detected by optically interrogating the device. Moreover, the device can be equipped with a temperature sensor to determine if the goods have been kept under recommended conditions. The on-board solar cell would allow the OFID device to stay active and record temperature even when it is not within range of a reader by harvesting ambient light energy.

In a smart home environment OFID devices could monitor variables such as temperature, noise, light intensity or human presence while their on-board solar cells harvested energy from ambient light (Fig. 9 (c)). The PL emissions of the solar cell can be modulated according to the sensed variables. If the room is dark or not well lit, the cell's EL emissions can be

modulated instead. A passive reader equipped with an imaging receiver can be employed to receive multiple transmissions and pinpoint their locations within the room.

OFID devices could be used to identify and track large objects such as shipping containers as they move through a port (Fig. 9 (d)). An active reader with a high-power collimated light beam, possibly from a laser source, could be used to interrogate the tag from a long distance. These OFID devices would not require active power from batteries, supporting their long-term and sustainable usage on objects used for transportation of goods such as shipping, trucking or railway containers.

IV. PHOTO-LUMINESCENCE MODULATOR CIRCUIT

We present and analyze a circuit that can both modulate PL emissions from a solar cell and harvest energy while boosting the voltage generated by the solar cell. Fig. 10 shows a system-level diagram of how this circuit (PL modulator & EH circuit) interfaces with a solar cell and a load (R_{load}). The device-to-reader input is a bit stream with data to be transmitted to a reader.

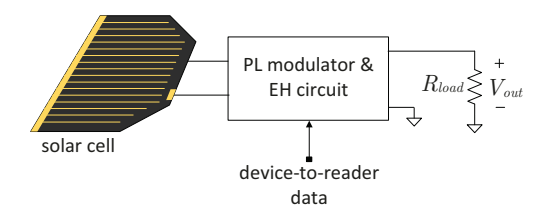


Fig. 10. System-level diagram of proof-of-concept circuit (PL modulator & EH circuit). This circuit is able to both modulate the PL emissions from a solar cell and harvest energy by transferring energy from the solar cell to the load R_{load} .

The PL modulator & EH circuits modulates PL emissions by varying the value of a resistance (R_{eq}) connected to the solar cell as shown in Fig. 11. Varying R_{eq} varies V_D and consequentially Φ_{lum} . Variations in R_{eq} are made according to the transmitted data.

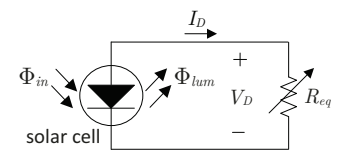


Fig. 11. Basic PL modulation principle. A variable resistor R_{eq} is connected to the solar cell. Varying R_{eq} varies V_D and consequentially Φ_{lum} .

From the circuit in Fig. 11 we can write:

$$I_{ph} + I_{s} = I_{s}e^{V_{D}(R_{sr} + R_{eq})/(nV_{T}R_{eq})} + \left(\frac{R_{sr} + R_{eq} + R_{sh}}{R_{eq}R_{sh}}\right)V_{D}$$
(7)

Equation (7) was solved numerically for $I_{ph}=20$ mA and its solution is shown graphically in Fig. 12 along with the relationship between V_D and R_{eq} . In the figure, the conditions $V_D=V_{oc}$ and $R_{eq}=R_{mpp}$, where $R_{mpp}=V_{mpp}/I_{mpp}$ is

the impedance of the solar cell at the MPP are highlighted. For this result, the following explicit expression for I_{mpp} was employed [14]:

$$I_{mpp} = I_{ph} + I_s - \frac{e(I_{ph} + I_s)}{W\left(\frac{e(I_{ph} + I_s)}{I_s}\right)}$$
(8)

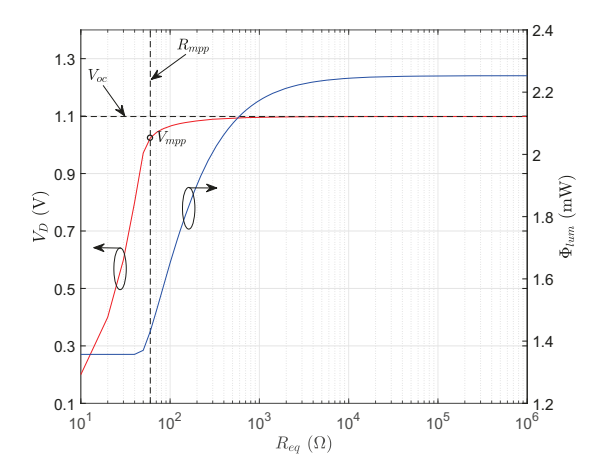


Fig. 12. Plot of the voltage across the solar cell V_D and the PL radiant flux Φ_{lum} as a function of R_{eq} . The conditions $V_D=V_{oc}$ and $R_{eq}=R_{mpp}$ are highlighted.

Notably, there is a rapid increase in Φ_{lum} for $R_{eq} > R_{mpp}$ with Φ_{lum} reaching 99.5% of its maximum OC value at $R_{eq} = 10^4~\Omega$. Based on this result, OOK modulation can be accomplished as follows: to transmit a logic high, set $R_{eq} = R_{mpp}$ and to transmit a logic low, set $R_{eq} > 10^4~\Omega$. Since $R_{eq} = R_{mpp}$ results in the maximum amount of energy drawn from the solar cell, when data is not being transmitted, R_{eq} should be set to R_{mpp} . PAM can be accomplished by varying R_{eq} in discrete steps in the range between R_{mpp} and $10^4~\Omega$.

Proposed Circuit:

Fig. 13 shows an implementation of the PL modulator & EH circuit. This circuit is based on a boost DC-DC converter. Transistor M_1 works as a switch and is driven by clock signal ϕ of frequency f_{sw} and duty cycle ρ . The circuit works in two phases: Phase 1 when ϕ is logic high and Phase 2 when ϕ is logic low. During Phase 1, M_1 closes connecting inductor L in parallel with the solar cell, charging the inductor. In Phase 2, M_1 opens and the inductor discharges through the Schottky diode D_s into the load R_{load} . During Phase 1 capacitor C_L feeds the load. The pulse width modulator generates a clock signal with duty cycle proportional to its input V_{mod} . d_{in} is a digital signal encoding the data being transmitted.

Fig. 13 shows d_{in} controlling V_{mod} and, therefore, the duty cycle of the DC-DC converter. The input impedance R_{in} of the DC-DC converter is a function of the duty cycle ρ . The duty cycle plays an important role in the operation of the DC-DC converter. The proper value of ρ enables the maximum energy transfer from the solar cell to the load.

Circuit Analysis:

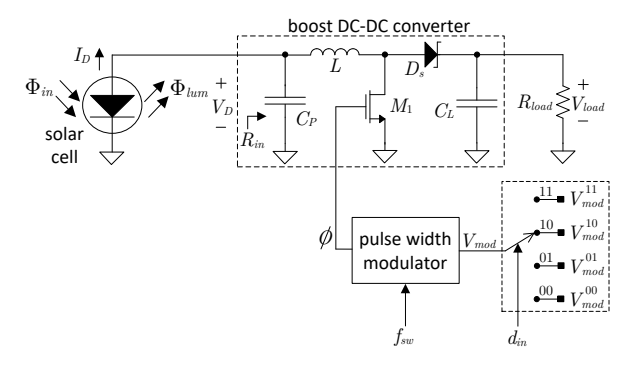


Fig. 13. Schematic diagram of proposed PL modulator & EH circuit. The circuit is based on a boost DC-DC converter and is able to both modulate the PL radiant flux Φ_{lum} and transfer energy from the solar cell to the load R_{load} while boosting the voltage of the solar cell. d_{in} is a digital signal encoding the data being transmitted.

An analysis of the proposed PL modulator & EH circuit is carried out here to gain a deeper insight of its operation and to guide its optimization. To simplify the analysis, the diode in the solar cell equivalent circuit of Fig. 2 is linearized using the first two Taylor series terms of its current-vs-voltage curve. The linearized solar cell equivalent circuit using this approach is shown in Fig. 14:

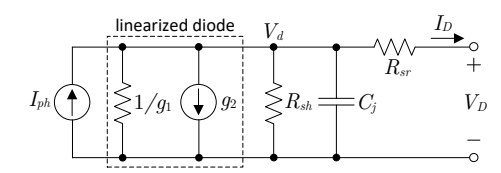


Fig. 14. Solar cell equivalent circuit with linearized diode.

where,

$$g_1 = \frac{I_s}{nVT} e^{V_{dm}/nV_T}$$

$$g_2 = I_s (e^{V_{dm}/nVT} - 1) - \frac{V_{dm}I_s}{nV_T} e^{V_{dm}/nVT}$$

$$(9)$$

and V_{dm} is the solar cell's DC operating point. Replacing the solar cell with its linearized equivalent in the PL modulator & EH circuit of Fig. 13 for Phase 1 (ϕ =high) of its operation yields the circuit shown in Fig. 15.

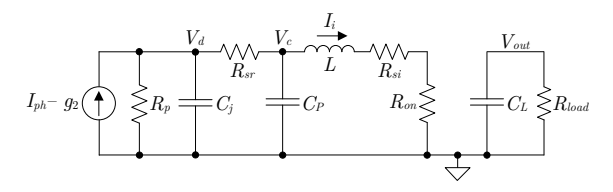


Fig. 15. Equivalent circuit of proposed circuit with linearized diode for Phase 1 ($\phi = \text{high}$).

In the figure, $R_P = R_{sh}/\!\!/(1/g_1)$, R_{si} is the series resistance of the inductor and R_{on} is the on resistance of M_1 . An analysis of this circuit yields the following set of differential equations:

$$\frac{dV_d}{dt} = -\frac{1}{C_j} \left(\frac{1}{R_P} + \frac{1}{R_{sr}} \right) V_d +$$

$$\frac{1}{C_j R_{sr}} V_c + \frac{I_{ph} - g_2}{C_j}$$

$$\frac{dV_c}{dt} = \frac{1}{C_P R_{sr}} V_d - \frac{1}{C_P R_{sr}} V_c - \frac{1}{C_P} I_i$$

$$\frac{dI_i}{dt} = -\frac{1}{L} V_c - \frac{R_{si} + R_{on}}{L} I_i$$

$$\frac{dV_{out}}{dt} = -\frac{1}{R_{load} C_L} V_{out}$$
(10)

An equivalent linear circuit for Phase 2 (ϕ =low) can be found in a similar manner. For Phase 2, we need to consider two different modes: Continuous Current Mode (CCM) and Discontinuous Current Mode (DCM). In CCM, the inductor L doesn't get fully discharged during Phase 2, i.e. the current through the inductor, I_i , remains greater than zero (I_i > 0). Fig. 16 shows the equivalent circuit during Phase 2 for CCM. V_{don} models the voltage drop across the Schottky diode.

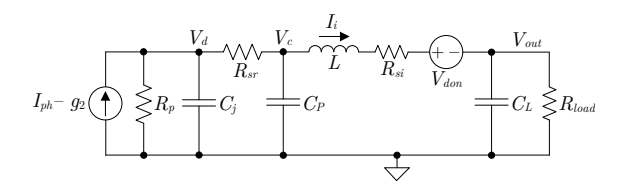


Fig. 16. Equivalent circuit of proposed circuit for Phase 2 and CCM ($\phi=$ low and $I_i>0$).

An analysis of the circuit in Fig. 16 yields the following set of differential equations:

$$\frac{dV_d}{dt} = -\frac{1}{C_j} \left(\frac{1}{R_P} + \frac{1}{R_{sr}} \right) V_d +$$

$$\frac{1}{C_j R_{sr}} V_c + \frac{I_{ph} - g_2}{C_j}$$

$$\frac{dV_c}{dt} = \frac{1}{C_P R_{sr}} V_d - \frac{1}{C_P R_{sr}} V_c - \frac{1}{C_P} I_i$$

$$\frac{dI_i}{dt} = -\frac{1}{L} V_c - \frac{1}{L} V_{out} - \frac{V_{don}}{L} - R_{si} I_i$$

$$\frac{dV_{out}}{dt} = \frac{1}{C_L} I_i - \frac{1}{R_{load} C_L} V_{out}$$
(11)

In DCM, the inductor gets fully discharged at some point during Phase 2. When this happens the diode D_s stops conducting isolating the load from the rest of circuit and preventing C_L from discharging through the inductor. Fig. 17 shows the equivalent circuit during Phase 2 for DCM.

An analysis of the circuit in Fig. 17 yields the following set of differential equations:

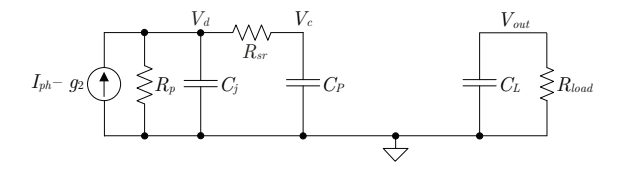


Fig. 17. Equivalent circuit of proposed circuit for Phase 2 in DCM (ϕ =low and $I_i = 0$).

$$\frac{dV_d}{dt} = -\frac{1}{C_j} \left(\frac{1}{R_P} + \frac{1}{R_{sr}} \right) V_d +$$

$$\frac{1}{C_j R_{sr}} V_c + \frac{I_{ph} - g_2}{C_j}$$

$$\frac{dV_c}{dt} = \frac{1}{C_P R_{sr}} V_d - \frac{1}{C_P R_{sr}} V_c$$

$$\frac{dV_{out}}{dt} = -\frac{1}{R_{load} C_L} V_{out}$$
(12)

Equations (11) to (13) were solved numerically using the Runge-Kutta method implemented in the **ode45**() function of MATLAB®. These equations were solved iteratively following the procedure shown in Fig. 18. In the figure, i.c. stands for initial conditions, f.c. stands for final conditions, $T_{sw} = 1/f_{sw}$, $T_1 = \rho T_{sw}$, $T_2 = (1 - \rho)T_{sw}$. T_{sim} is the simulation time

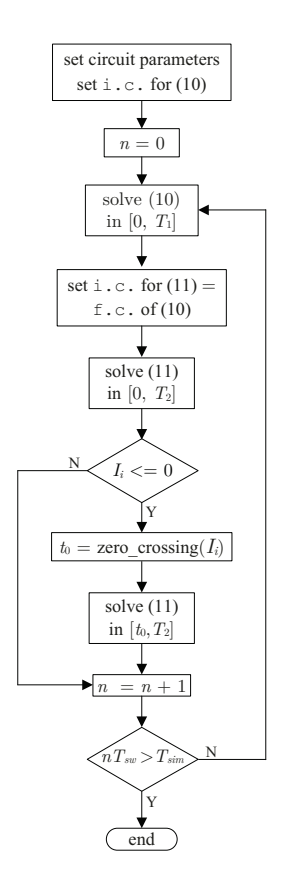


Fig. 18. Flow diagram showing iterative procedure employed to find the solutions for $V_d,\,V_c,\,I_i$ and $V_{out}.$

Using the method described above, the equations describing the DC-DC converter were solved for three different values of I_{ph} (10, 15 and 20 mA) and for $L=68~\mu\mathrm{H},~R_{si}=1.0~\Omega,~C_P=10~\mu\mathrm{F},~R_{on}=0.3~\Omega,~f_{clk}=40~\mathrm{kHz},~V_{don}=0.3~\mathrm{V},~R_{sr}=1~\Omega,~C_j=550~\mathrm{nF},~R_{load}=5~\mathrm{k}\Omega$ and $T_{sim}=200~\mathrm{ms}.$ Fig. 19 shows the resulting average output voltage \overline{V}_{out} as the duty cycle ρ is varied. Notably, the duty cycle at which the output voltage peaks, i.e. maximum power is transferred to the load, varies with the photo-current I_{ph} . Setting the duty cycle such that maximum power is transferred to the load is the function of an MPP controller.

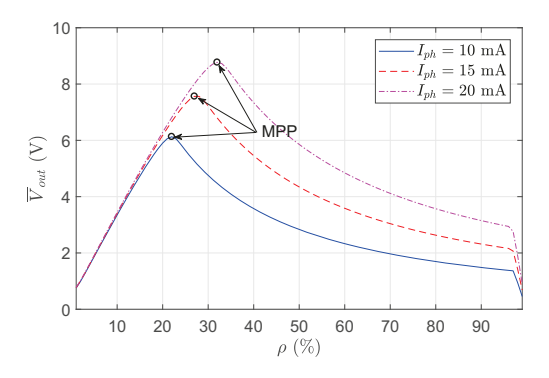


Fig. 19. Average output voltage of DC-DC converter, \overline{V}_{out} , as a function of the duty cycle ρ .

We will approximate the input impedance of the DC-DC converter, R_{in} , in the following manner:

$$R_{in} = \frac{\overline{V}_c}{\left(\frac{Q_i}{T_{sw}}\right)} \tag{13}$$

where, \overline{V}_c is the average V_c voltage and Q_i is the charge drawn by the inductor in one clock cycle. Assuming a linear profile for the inductor current during Phase 1 (inductor charging) and letting I_{i1} and I_{i2} be the inductor currents at the beginning of phases 1 and 2, respectively, we can write:

$$Q_{i} = \int_{0}^{T_{1}} \left(I_{i1} + \frac{I_{i2} - I_{i1}}{T_{1}} \right) dt = I_{i1}T_{1} + \frac{T_{1}}{2} \left(I_{i2} - I_{i1} \right)$$
(14)

Replacing (14) in (13) and using the values of \overline{V}_c , I_{i2} and I_{i1} obtained from solving the equation describing the DC-DC converter, yields the relationship between R_{in} and ρ shown in Fig. 20. In the figure, the impedance of the solar cell at the MPP, R_{mpp} , is marked for $I_{ph}=10$, 15 and 20 mA. Notably, an input impedance greater than $10^4~\Omega$ is achieved for $\rho \leq 2.5\%$.

Finally, combining the Φ_{lum} vs. R_{eq} and the R_{in} vs. ρ relationships given in Figs. 12 and 20, yields the relationship Φ_{lum} vs. ρ shown in Fig. 21. This figure shows that the PL radiant flux of a solar cell can be modulated by varying the duty cycle of the DC-DC converter.

The efficiency of the boost DC-DC converter can be improved by replacing the Schottky diode with an active diode circuit in order to reduce the losses due to the voltage drop across the Schottky diode. An active diode circuit consists of a MOSFET and a voltage comparator [24]. The comparator turns off the MOSFET when its drain-to-source voltage becomes negative. Although the comparator consumes additional power, an on-chip low-power implementation of a DC-DC converter

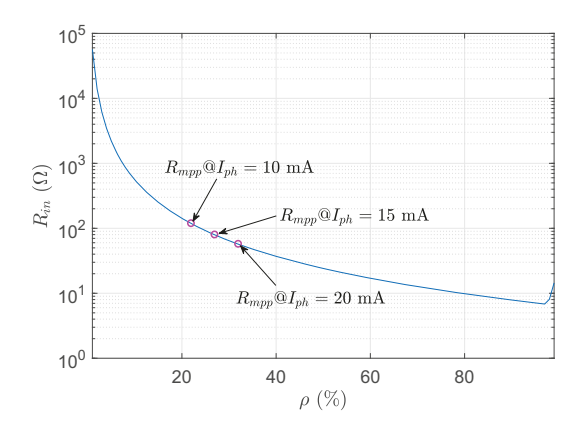


Fig. 20. Relationship between the input impedance of the DC-DC converter, R_{in} , and the duty cycle of the clock signal ρ . The impedance of the solar cell at the MPP, R_{mpp} , is marked for $I_{ph}=10$, 15 and 20 mA

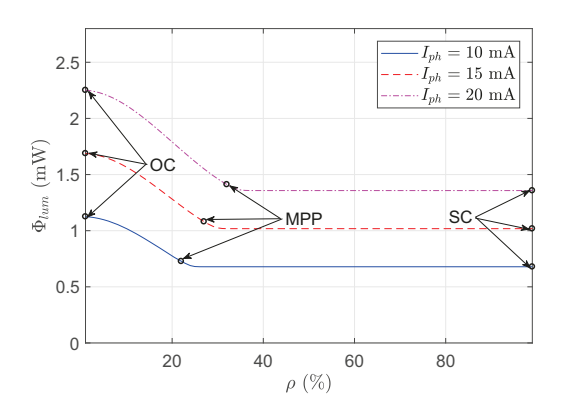


Fig. 21. Relationship between the luminescent radiant flux of a solar cell, Φ_{lum} , and the duty cycle of the DC-DC converter, ρ , for different values of the photo-current I_{ph} .

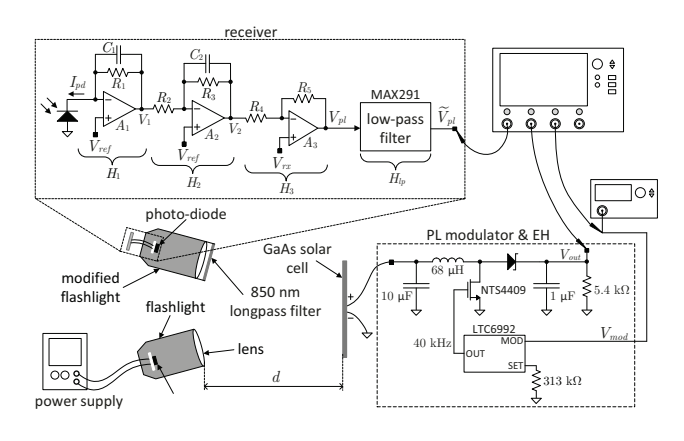
with an active diode is more efficient than an implementation with discrete components [25].

We have observed that GaN blue and green LEDs have a strong PL response when illuminated with violet light (405 nm). This PL response is also a function of the impedance across the LED. Hence, the proposed PL modulator & EH circuit can be used to modulate the PL emissions of GaN blue and green LEDs. Typically, LEDs have much smaller active areas and higher cost (per unit area) than solar cells. Thus, using LEDs for OFID devices would make sense in applications where highly directed and concentrated light beams can be used.

V. RESULTS

The PL modulator & EH circuit was built and tested to verify its functionality and the validity of the analytical model presented in Section IV. Fig 22(a) shows the schematic diagram of the test setup that was employed for these tests. Fig. 22(a) shows a photograph of the test setup. A GaAs solar cell from Alta Devices was placed in front of a flashlight with a red (623 nm) LED at a distance d=12 cm. The current through the LED was adjusted such that the photo-generated current in the solar cell, I_{ph} , was 20 mA.

A second flashlight, modified to hold a photo-diode and an amplifier instead of an LED, was also placed in front of the



modified flashlight generator flashlight PL modulator & EH

(a)

Fig. 22. Experimental setup employed to test the functionality of the proposed circuit and the validity of the developed analytical model. (a) Schematic diagram; (b) Photograph of entire system. The insets show a closeup view of the fabricated circuits.

(b)

solar cell. The photo-diode's current, I_{pd} , is converted to a voltage by a trans-impedance amplifier and further amplified to produce the voltage V_{pl} , which is proportional to I_{pd} . An oscilloscope was employed to record the V_{pl} , V_{mod} and V_{out} waveforms. The photo-diode's current is a function of the solar cell's luminescent radiant flux at distance d, $\Phi_{lum}(d)$, as follows:

$$I_{nd} = R_{nd} \ \Phi_{lum}(d) \tag{15}$$

where, R_{pd} is the responsivity of the photo-diode in A/W. Given that $\Phi_{lum}(d) \propto \Phi_{lum}$, we conclude that $V_{pl} \propto \Phi_{lum}$. Hence, the V_{pl} waveforms recorded by the oscilloscope are proportional to the luminescent radiant flux emitted by the solar cell.

The clock signal for the PL modulator & EH circuit is provided by a voltage-controlled pulse width modulator circuit (LTC6992 from Linear Technology). The duty cycle of the clock signal generated by this circuit is a linear function of the voltage V_{mod} with $V_{mod}=95$ mV corresponding to $\rho=0\%$ duty cycle and $V_{mod}=900$ mV corresponding to $\rho=100\%$ duty cycle. The switching frequency was set to 40 kHz. The receiver circuit (at the reader side) consists of a transimpedance amplifier (TIA), two inverting amplification stages

and a low-pass filter. The low-pass filter removes the ripple noise caused by the switching action of the DC-DC converter. This filter was implemented with an 8^{th} order Butterworth low-pass filter (MAX291 from Maxim Integrated) with a cutoff frequency set to 20 kHz. Other parameters of the receiver were set as follows: $R_1=100~\text{k}\Omega,~C_1=11~\text{pF},~R_2=10~\text{k}\Omega,~C_2=62~\text{pF},~R_3=1~\text{M}\Omega,~R_4=9.8~\text{k}\Omega,~R_5=9.8~\text{k}\Omega$ and $V_{ref}=1.5~\text{V}.$

The first test conducted involved sweeping V_{mod} from 95 mV to 900 mV to observe the effects of duty cycle change on V_{pl} and on the output of the DC-DC converter, V_{out} . Fig. 23 shows the recorded V_{mod} , V_{pl} and V_{out} waveforms.

The inset shows a closeup view of the ripple noise in V_{pl} . This noise is due to the switching action of the DC-DC converter. The dotted line is the low-pass version of V_{pl} with the ripple removed. Notably, V_{pl} , which is proportional to Φ_{lum} , achieves its maximum for $\rho=0\%$ or $V_{mod}=95$ mV (OC) and its minimum for $\rho=100\%$ or $V_{mod}=900$ mV (SC). The MPP, which is the point at which V_{out} is maximum is achieved for $V_{mod}=355$ mV or $\rho=32.7\%$ duty cycle. The location of the MPP and the overall behavior of V_{out} with respect to ρ is in good agreement with the results presented in Fig. 19.

The V_{pl} waveform (after ripple noise was removed) is also in good agreement with the relationship between Φ_{lum} and the duty cycle ρ presented in Fig. 21. At the MPP, $V_{out}=8$ V, resulting in 11.9 mW of power delivered to the load. Considering that for $I_{ph}=20$ mA, $V_{pp}\times I_{mpp}=17.7$ mW, the efficiency of the DC-DC converter, at the MPP, is 67%.

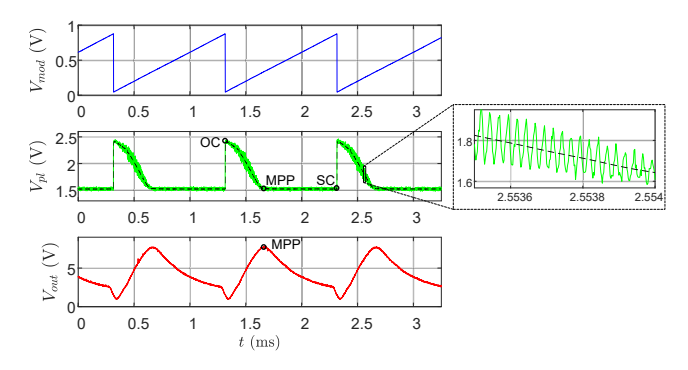


Fig. 23. Recorded waveforms $(V_{mod}, V_{pl} \text{ and } V_{out})$ from the experimental setup. As V_{mod} is swept from 95 mV to 900 mV, the duty cycle, ρ , varies linearly from 0% to 100%. At $\rho=32.7\%$ $(V_{mod}=355 \text{ mV})$, V_{out} achieves its maximum value (MPP). The inset shows a closeup of the ripple noise in V_{pl} . The dotted line is a low-pass version of V_{pl} with the ripple removed. The open circuit $(\rho=0\%)$ and the short circuit $(\rho=100\%)$ points are marked with OC and SC, respectively

A second test that consisted in varying the amplitude of the emitted PL radiant flux in discrete steps was carried out. This test shows the possibility of using PAM to transmit digital information with PL emissions of a solar cell. To this end, V_{mod} was varied in 8 discrete levels (with each level corresponding to a digital symbol) ranging from 95 mV (OC) to 355 mV (MPP). Due to the non-linear relationship between Φ_{lum} and ρ , these levels were not equally spaced. Table I lists the V_{mod} voltage values and the corresponding duty cycles assigned to each symbol.

TABLE I $V_{mod} \text{ and } \rho \text{ values for transmitted symbols}$

	Symbol	V_{mod} (mV)	ρ (%)
	000	95	0
	001	165	8.7
	010	210	14.7
	011	240	18.7
	100	260	21.3
	101	285	24.4
	110	315	28.1
	111	355	32.7

Fig. 24 shows the V_{mod} , V_{pl} and V_{out} waveforms recorded by the oscilloscope for this test. The inset shows a closeup view of the ripple noise in V_{pl} . At the receiver side this noise is removed by the low-pass filter for reliable reception of the transmitted symbols.

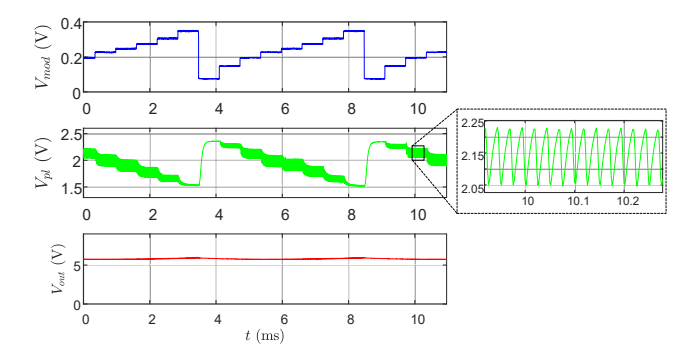


Fig. 24. Recorded waveforms when V_{mod} is varied in 8 discrete levels ranging from $V_{mod}=95~\mathrm{mV}$ (OC) to $V_{mod}=355~\mathrm{mV}$ (MPP). The inset shows a closeup view of the ripple noise on V_{pl} .

Fig. 25 shows the output of the low-pass filter V_{pl} . A cleaner signal with the 8 discrete levels clearly distinguishable can be seen. In this test, the duration of each symbol was set to 0.625 ms, which would result in a transmission speed of 4.8 kbps. Fig. 24 also shows that the output of the DC-DC converter dropped to 5.99 V (as a result of the modulation) resulting in 6.54 mW of power delivered to the load. This drop is due to the fact that, in order to modulate the PL emissions of the solar cell by varying the input impedance of the DC-DC converter, the DC-DC converter does not always operate at the MPP. This result illustrates an inherent tradeoff in the proposed PL modulator & EH circuit, namely, the ability of harvesting maximum power is traded with the ability of transmitting information. Depending on the requirements of the target application, either power harvesting or information transmission may be maximized. For instance, to maximize power harvesting while transmitting information, the variations in duty cycle should be kept close to the MPP. This would mean that either: 1) fewer discrete levels (symbols) are transmitted per unit time or 2) the spacing between each level is reduced. In either case the transmission of information is hindered by a reduction of the transmission rate or a reduction of the signal-to-noise ratio.

Another test was carried out to demonstrate the performance of OOK modulation. In this test the PL radiant flux was modulated by flipping V_{mod} between 95 mV (OC) and 355

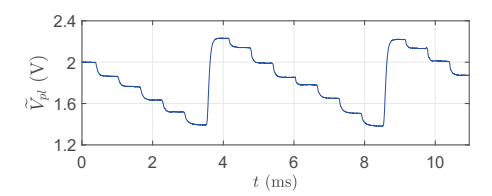


Fig. 25. Output of the $8^{\rm th}$ order low-pass filter. The ripple noise in V_{pl} is effectively removed by low-pass filter yielding a cleaner signal in which the 8 discrete transmitted levels are distinguishable.

mV (MPP). Fig. 26 shows the recorded V_{pl} waveforms for three different modulation frequencies: 1 kHz (top row), 5 kHz (middle row) and 10 kHz (bottom row).

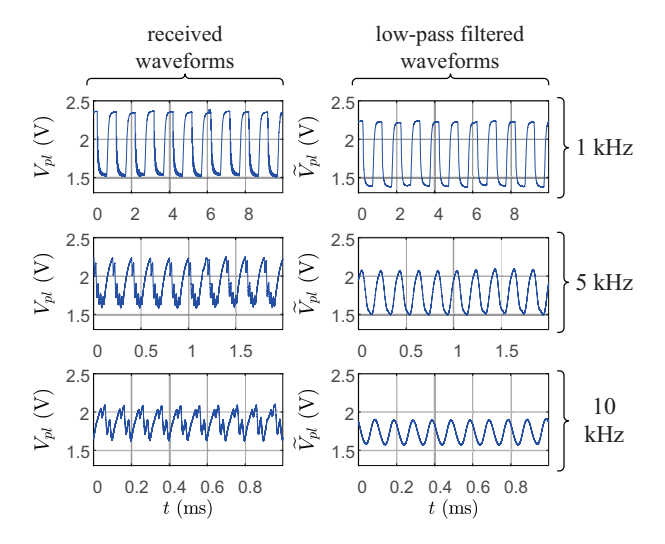


Fig. 26. Recorded V_{pl} waveforms for OOK modulation for three modulating frequencies: 1 kHz (top row), 5 kHz (middle row) and 10 kHz (bottom row).

As the modulation frequency increases, the amplitude of V_{pl} decreases. This decrease in amplitude is due to capacitor C_P which limits how fast the DC-DC converter can reach its steady state after a change in the duty cycle. This is another trade-off in the PL modulator & EH circuit. On one hand, the value of C_P should be increased to maximize the output voltage of the DC-DC converter. For instance, at a modulating frequency of 5 kHz, the average output voltage of the DC-DC converter is 6.20 V for $C_P=10~\mu\mathrm{F}$, 5.57 V for $C_P=0~\mu\mathrm{F}$ and 6.59 V for $C_P=470~\mu\mathrm{F}$. Depending on the requirements of the target applications, the value of C_P should be set to either maximize harvested power or the transmission bandwidth.

Receiver Circuit

An analysis of the receiver circuit shown in Fig. 22 is presented here to provide an insight into its performance. The transfer function of the receiver, H_{rcv} , can be expressed as the product of the transfer function of the amplification stages and the low-pass filter as follows:

$$H_{rcv}(s) = H_1(s) \times H_2(s) \times H_3(s) \times H_{ln}(s)$$
 (16)

where, H_1 , H_2 , H_3 and H_{lp} are the transfer functions of the TIA, the inverting amplifiers and the low-pass filter,

respectively. From the circuit diagram in Fig. 22(a) we can write:

$$H_1(s) = \frac{v_1}{i_{pd}} = \left(\frac{R_1}{1 + sR_1C_1}\right) \left(\frac{A(s)}{1 + A(s)}\right)$$
(17)

$$H_2(s) = \frac{v_2}{v_1} = \frac{-R_3A(s)}{R_2(1 + A(s))(1 + sR_2C_2) + R_3}$$

$$H_3(s) = \frac{v_{pl}}{v_2} = \frac{-R_5A(s)}{R_4(1 + A(s)) + R_5}$$

where, i_{pd} , v_1 , v_2 and v_{pl} are the small signal components of I_{pd} , V_1 , V_2 and V_{pl} , respectively. A(s) is the open-loop transfer function of the opamps, which will be approximated with a first-order transfer function as follows:

$$A(s) = \frac{A_0}{1 + \frac{s}{\omega_0}} \tag{18}$$

where, A_0 is the DC gain and ω_0 is the corner frequency of the opamps. The transfer function of the low-pass filter is given by:

$$H_{lp}(s) = \frac{1}{1 + \left(\frac{s}{\omega_c}\right)^n}.$$
 (19)

where, n is the filter order and ω_c is the corner frequency.

Replacing (17), (18) and (19) in (16) and setting $s=j\omega$, $A_0=120$ dB, $\omega_0=188.5$ rad/s (30 Hz), n=8, and $\omega_c=1.25\times 10^5$ rad/s (20 kHz) yields the frequency response of the receiver circuit. Fig. 27 (top) shows the magnitude of the frequency response of the receiver.

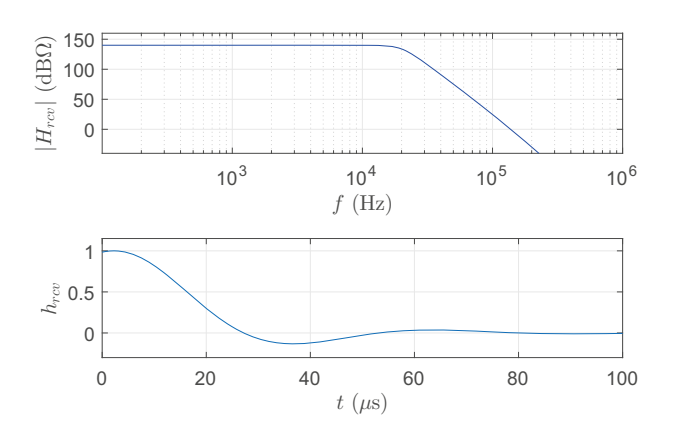


Fig. 27. Magnitude of the frequency response of receiver circuit (top) and impulse response of receiver circuit (bottom).

The impulse response, h_{rcv} , of the receiver can be obtained by computing the inverse Fourier transform of the frequency response. The normalized impulse response is shown in Fig. 27 (bottom). Notably, the impulse response goes down to zero after approximately 80 μ s. Hence, to avoid inter-symbol interference (ISI), the maximum bit rate that can be achieved with this receiver is around 12.5 kbps. The low-pass filter contributes with the dominant pole of the frequency response. Since the corner frequency of the low-pass filter should not he higher than the switching frequency of the DC-DC converter, to increase the speed of the receiver, the switching frequency of the DC-DC converter will have to be increased. However, the switching frequency cannot be increased indefinitely.

At very high frequencies, power losses due to circuit nonidealities such as the MOSFET's non-zero switching time, parasitic capacitances and the frequency-dependent power dissipation of the clock generator will outweigh the power generated by the DC-DC converter.

Communication Performance

The bit error rate (BER) achieved with the PL modulator for OOK modulation was measured to assess the performance of the overall OFID communication system. For these measurements the output of the low-pass filter, V_{out} , was fed to a comparator to generate back a fully digital signal. An FPGA was employed to implement a pseudo random bit generator (PRBG) and the clock signal of 40 kHz with variable duty cycle needed to control the DC-DC converter. The duty cycle of this clock signal was set to the duty cycle corresponding to the MPP if the output of the PRGB was logic high and 0% (OC) if the output of the PRGB was logic low. The BER was calculated as the ratio between the number of times the outputs of the PRGB and the comparator were different over the total number of generated bits, which was set to 10^6 bits. The BER and the power delivered to the load, P_{load} , were recorded for different distances d. The bit rate was set to 10 kbps, which is right below the maximum bit rate for ISI-free communications. The gain of the third amplification stage of the receiver was set to 10.

Fig. 28 shows the measurement results. At d=50 cm the BER is 1.6×10^{-3} , well within the limits of forward error correction [23]. However, at distances greater than 50 cm the BER increases rapidly. The power delivered to the load at 12 cm is 7.15 mW and at 50 cm is 5.22 mW resulting in an end-to-end power harvesting efficiency of 40% and 29%, respectively.

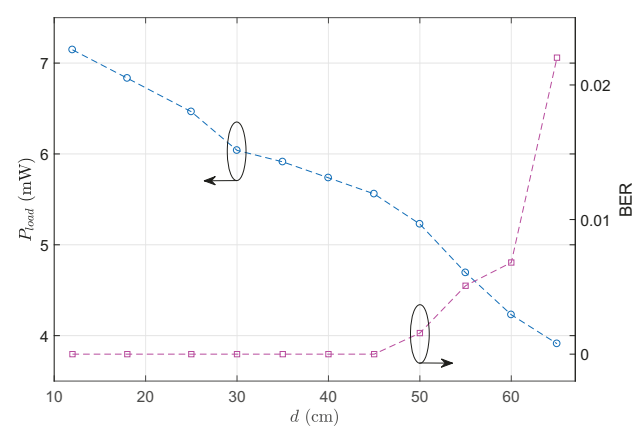


Fig. 28. Measured BER and P_{load} as a function of distance between the reader and the solar cell.

VI. CONCLUSION

An optical communication scheme that employs solar cells to transmit information has been presented. In this scheme, the luminescence emissions of high-efficiency solar cells, such as GaAs solar cells, are modulated with information. A device equipped with this type of solar cells can use

it, not only to harvest ambient energy, but also to transmit and receive information. This scheme was compared with RFID technology and possible applications were described. A circuit suitable for modulating the PL emissions of a solar cell was proposed and analyzed. Test results from a hardware implementation of this circuit showed that it can be used to implement PAM and OOK modulation. It was shown that a trade-off exists in this circuit between energy harvesting and information transmission. Harvested energy is maximized when no information is transmitted, whereas, information transmission comes at a cost of a drop in harvested energy. The target application will ultimately dictate how to balance this trade-off.

Future work in the area of OFID includes: finding optimum modulation and encoding schemes, establishing the radiated power level and wavelength (from the reader) that maximize reading distance, developing low-power integrated circuits that integrate most or all the functionalities of an OFID device, designing optical systems for the reader that maximize reading distances while minimizing the reader size and the implementation of imaging receivers and decoders.

ACKNOWLEDGMENT

This work was supported in part by the National Science Foundation.

REFERENCES

- [1] O. D. Miller, E. Yablonovitch and S. R. Kurtz, "Strong internal and external luminescence as solar cells approach the Schockley-Queisser limit," *IEEE Journal of Photovoltaics*, vol. 2, no. 3, pp. 303-311, 2012.
- [2] J. M. Raguse and J. R. Sites, "Correlation of electroluminescence with open-circuit voltage from thin-film CdTe solar cells," *IEEE Journal of Photovoltaics*, vol. 5, no. 4, pp. 1175-1178, 2015.
- [3] K. Schick, E. Daub, S. Finkbeiner and P. Würfel, "Verification of a generalized Planck law for luminescence radiation from silicon solar cells," *Applied Physics A*, vol. 54, pp. 109-114, 1992.
- [4] U. Rau, "Reciprocity relation between photovoltaic quantum efficiency and electroluminescence emission of solar cells," *Physical Review B*, vol. 76, pp. 085303-1–085303-8, 2007.
- [5] Z. Meng and Z. Li, "RFID tag as a sensor a review of the innovative designs and applications," *Measurement Science Review*, vol. 16, no. 6, pp. 305-315, 2016.
- [6] W. D. Leon-Salas and C. Halmen, "A RFID sensor for corrosion monitoring in concrete," *IEEE Sensors Journal*, vol. 16, no. 1, pp. 32-42, 2016.
- [7] S. Zhang, D. Tsonev, S. Videv, S. Ghosh, G. A. Turnbull, I. F. W. Samuel and H. Haas, "Organic solar cells as high-speed data detectors for visible light communications," *Optica*, vol. 2, no. 7, pp. 607-610, 2015.
- [8] Z. Wang, D. Tsonev, S. Videv and H. Haas, "On the design of a solar-panel receiver for optical wireless communications with simultaneous energy harvesting," *IEEE Journal on Selected Areas in Communications*, vol. 33, no. 8, pp. 1612-1623, 2015.
- [9] Y. Liu, H.-Y. Chen, K. Liang, C.-W. Hsu, C.-W. Chow and C.-H. Yen, "Visible light communication using communication using receivers of camera image sensor and solar cell," *IEEE Photonics Journal*, vol. 8, no. 1, pp. 1-7, 2016.
- [10] M. Gorlatova, P. Kinget, I. Kymissis, D. Rubenstein, X. Wang and G. Zussman, "Energy harvesting active networked tags (EnHANTs) for ubiquitous object networking," *IEEE Wireless Communications*, vol. 17, no. 6, pp. 1536-1284, 2010.
- [11] E. Welbourne et al., "Building the Internet of Things using RFID," IEEE Internet Computing, vol. 13, no. 3, 2009.
- [12] A. Al-Fuaqba et al., "Internet of things: a survey on enabling technologies, protocols and applications," *IEEE Communication Surveys and Tutorials*, vol. 17, no. 4, pp. 2347-2376, 2015.
- [13] W. D. Leon-Salas and X. Fan, "Exploiting luminescence emissions of solar cells for Optical Frequency Identification (OFID)," *IEEE Interna*tional Symposium on Circuits and Systems (ISCAS), 2018.

- [14] S. Ghosh, H.-T. Wang and W. D. Leon-Salas, "A circuit for energy harvesting using on-chip solar cells," *IEEE Transactions on Power Electronics*, vol. 29, no. 9, pp. 4658-4671, 2014.
- [15] R. M. Corless, G. H. Gonnet, D. E. G. Hare, D. J. Jeffrey and D. E. Knuth, "On the Lambert W function," Adv. Comput. Math., vol. 5, pp. 329-359, 1996.
- [16] Alta Devices, "The world's most efficient solar". [Online]. Available: https://www.altadevices.com. [Accessed April 2018].
- [17] B. Warneke, M. Last, B. Liebowitz and K. S. J. Pister, "Smart Dust: communicating with a cubic-millimeter computer," *Computer*, vol. 34, no. 1, pp. 44-51, 2001.
- [18] K. Finkenzeller, RFID handbook, third edition, John Wiley & Sons, 2010.
- [19] G. Benelli, A. Pozzebon, M. B. I. Reaz, "RFID under water: technical issues and applications," in *Radio Frequency Indentification from System* to Applications, pp. 379-395, 2013.
- [20] H. Elgala, R. Mesleh and H. Hass, "Indoor optical wireless communication: potential and state-of-the-art," *IEEE Communications Magazine*, vol. 49, on. 9, pp. 56-62, 2011.
- [21] RFID Journal, "Meco uses plating to cut antenna costs". [Online]. Available: https://www.rfidjournal.com/articles/view?1452. [Accessed August 2018]
- [22] T. Çiftçi, B. Karaosmanoğlu and Ö. Ergül, "Low-cost inkjet antennas for RFID applications," *IOP Conf. Ser.: Mater. Sci. Eng.*, vol. 120, 2016.
- [23] ITU-T. (2004). Forward error correction for high bit-rate DWDM sub-marine systems, ITU, Geneva, Switzerland, Tech. Rep. ITU-T G.975.1, Accessed May 6, 2018. [Online]. Available: https://www.itu.int/rec/T-REC-G.975.1-200402-I/en.
- [24] Y.-H. Lam, W.-H. Ki and C.-Y. Tsui, "Integrated low-loss CMOS active rectifier for wirelessly powered devices," *IEEE Transactions on Circuits* and Systems-II, vol. 53, no. 12, pp. 1378-1382, 2006.
- [25] R. D. Prabha and G. A. Rincon-Mora, "0.18-μm light-harvesting battery-assisted charger-supply CMOS system," *IEEE Transactions on Power Electronics*, vol. 31, no. 4, pp. 2950-2958, 2016.

PLACE PHOTO HERE Walter D. Leon-Salas received the B.S. degree in electronic engineering from Universidad Nacional de San Agustín, Arequipa, Peru. He received the M.S. and Ph.D. degrees in electrical engineering from the University of Nebraska-Lincoln (UNL) in 2001 and 2006, respectively. From 2007 to 2012 he was with the University of Missouri-Kansas City. In 2011 he received the CAREER award from the National Science Foundation and the Leadership Excellence Achievement Program (LEAP) Award from the Missouri Society of Professional Engineers. Currently he

is with the School of Engineering Technology at Purdue University where he is an Associate Professor. His research interests include optical communications using solar cells, CMOS imaging, data compression and energy harvesting.

PLACE PHOTO HERE Xiaozhe Fan was born in China. He received the Bachelor of Science degree from Tianjin University of Science and Technology, Tianjin, China in June 2013, and the Masters degree in electrical engineering technology from Purdue University, West Lafayette, IN, USA in August 2016. He is currently working toward the Ph.D. degree in electrical and computer engineering technology at Purdue University, West Lafayette, IN, USA. His research interests include optical frequency identification (OFID) technology, energy harvesting, and self-powered wireless

sensor applications.